Appl. Phys. A (2015) 120:745–755
DOI 10.1007/s00339-015-9252-7

Applied Physics A
Materials Science & Processing

# Structural, microstructural, and optical properties of $Zn_{1-x}Mg_xO$ thin films grown onto glass substrate by ultrasonic spray pyrolysis

**K. Hoggas[1] · Corinne Nouveau[2] · A. Djelloul[1] · M. Bououdina[3]**

Received: 20 May 2015 / Accepted: 21 May 2015 / Published online: 28 May 2015


**Abstract** Pure and doped $Zn_{1-x}Mg_xO$ films were deposited onto glass substrate by ultrasonic spray pyrolysis technique. The variation of lattice constant and the blue shift of near-band-edge emission indicate that $Zn^{2+}$ ions are successfully substituted by $Mg^{2+}$ ions within ZnO lattice. At higher Mg content ($x \geq 0.21$), a drastic change appears in the morphology, as a result of structural changes from wurtzite (ZnO) structure into a mixture of wurtzite and cubic (MgO) phases. FTIR study indicated the existence of distinct characteristic absorption peaks at $\sim$442 $cm^{-1}$ for Zn–O stretching mode that shifted toward the red region with the increase in Mg content. In addition to the host phonons of ZnO, one additional band was observed around 523 $cm^{-1}$, presumably attributed to the Mg-related vibrational mode. The optical constants and thickness of thin films have been determined using experimental transmittance data. The luminescence intensity at 2.63 eV of $Zn_{0.85}Mg_{0.15}O$ thin films was found to be approximately 13 times higher than that of pure ZnO film measured under the same excitation conditions.

✉ M. Bououdina
mboudina@gmail.com

[1] Laboratoire des Structures, Propriétés et Interactions Inter Atomiques (LASPI2A), Khenchela University, Khenchela, Algeria

[2] Laboratoire Bourguignon des Matériaux et Procédés, CER Arts et Métiers ParisTech of Cluny, 71250 Cluny, France

[3] Department of Physics, College of Science, University of Bahrain, PO Box 32038, Zallaq, Kingdom of Bahrain

## 1 Introduction

Zinc oxide (ZnO), a wide-bandgap ($E_g = 3.37$ eV) semiconductor, has attracted considerable attention as a promising candidate for ultraviolet optical applications such as laser diodes and light-emitting diodes. In comparison with GaN, ZnO has a large free exciton binding energy of 60 meV and a small Bohr radius of 1.8 nm [1], which might lead to reliable high-efficiency and high-speed photonic devices [2–4]. Moreover, ZnO is more resistant to radiation damage than some others semiconducting materials [5]. The growth of heterostructures and quantum wells for band gap engineering is considered as one of the key issues that need to be addressed in applications for UV optoelectronics.

One of the most interesting features of ZnO is the possibility of tuning its band gap by substituting Zn by some bivalent metals such as Cd and Mg. On the other hand, MgO is the prototype of an ionic compound semiconductor with wide band gap of 7.8 eV; therefore, Mg substitution within ZnO lattice would lead to an increase in the band gap depending on the Mg concentration [6].

The addition of impurities among the wide-bandgap semiconductors often induces dramatic changes in their structural and optical properties. For example, ternary $Zn_{1-x}Cd_xO$ system has an energy gap lower than that of ZnO, thus it can serve as an active layer for light emission in the visible range because of the smaller direct band gap of CdO of 2.3 eV [7]. On the opposite side, the value of the energy gap of ternary $Zn_{1-x}Be_xO$ can be efficiently engineered to values larger than that of ZnO, because of the larger band gap of BeO (10.6 eV) [8]. $Zn_{1-x}Mg_xO$ system can be considered as another potential candidate to develop ZnO-based semiconductors having an energy gap larger than that of ZnO. The value of the optical band gap energy

of the hexagonal $Zn_{1-x}Mg_xO$ films can be tunable from 3.3 to 4.0 eV at room temperature as the content of Mg is increased up to $x = 0.33$ [6].

Over the last decade, $Zn_{1-x}Mg_xO$ films have attracted an increasing interest as an alternative Cd-free buffer material for CIGS solar cells [9, 10]. It has been reported that $Zn_{1-x}Mg_xO$ film offers several advantages, including its variable band gap value. Indeed, the band gap can be adjusted within the range 3.2–3.9 eV simply by controlling the chemical composition of the ternary compound [11, 12]. The thermodynamic limit solid solubility of MgO in ZnO is reported around 4 % in the bulk [13]. However, the limit solid solubility of MgO in ZnO for thin films has been reported to be around 33 mol % as deposited by pulsed laser deposition (PLD) technique [6], 25 % as deposited by sol–gel spin-coating technique [14] and 43 % as deposited by molecular beam epitaxy (MBE) [15].

Since the crystal structure of ZnO and MgO is wurtzite (hexagonal) and rock salt (cubic), respectively, the solubility limit of Mg in ZnO would depend on the growth mechanisms as well as growth conditions [4, 15, 16].

In this work, $Zn_{1-x}Mg_xO$ films were successfully synthesized onto glass substrate by ultrasonic spray pyrolysis (USP). The crystallinity and the optical properties of the as-fabricated films have been investigated by X-ray diffraction (XRD), scanning electron microscopy (SEM), energy-dispersive X-ray analysis (EDS), Fourier transform infrared (FTIR) spectroscopy, UV visible spectroscopy, and photoluminescence (PL). The structural and optical properties of the $Zn_{1-x}Mg_xO$ films were discussed as a function of Mg content.

## 2 Experimental details

### 2.1 Films preparation

$Zn_{1-x}Mg_xO$ films with different Mg content were deposited by USP under ambient atmosphere. Two kinds of aqueous solutions, $Zn(CH_3COO)_2.2H_2O$ (AR) and $Mg(CH_3COO)_2.4H_2O$ (AR), were chosen as the sources of zinc and magnesium, respectively. In order to obtain $Zn_{1-x}Mg_xO$ films with different Mg contents ($0 \leq x \leq 0.3$), the solution had the following amounts: 0.01 M of zinc acetate; 50 ml deionized water (resistivity = 18.2 MΩ cm); 20 ml $CH_3OH$ (Merck 99.5 %); 30 ml $C_2H_5OH$ (Merck 99.5 %); and 10–30 % (Mg, at.%) magnesium acetate tetrahydrate. A small amount of acetic acid was added to aqueous solutions to adjust the pH value to about 4.8 in order to prevent the formation of hydroxides. Water is the most convenient oxidizing agent. Methanol and ethanol were the obvious choice because of their volatility and thus facilitating quick transformation of the precursor mist into vapor form, which is an important criterion for obtaining good-quality films. The ultrasonic spraying system used in this work consists of a commercial ultrasonic atomizer VCX 134 AT and a substrate holder with heater. The ultrasonic vibrator frequency was 40 kHz, and the used power was 130 W. The median drop size at 40 kHz is of 45 µ. The nozzle to substrate distance was fixed at 5 cm and during the deposition, the solution flow rate was held constant at 0.1 ml/min. $Zn_{1-x}Mg_xO$ thin films were deposited onto microscope cover glass substrates ($30 \times 12 \times 1.2$ mm$^3$) at 450 °C. The deposition time was 30–45 min. The substrate temperature was monitored with a thermocouple and controlled electronically.

### 2.2 Films characterisations

The film morphology was examined using JEOL JSM7600F scanning electron microscope (SEM). The chemical composition was determined using energy-dispersive spectroscopy (EDS) analysis. The structural analysis was performed by powder XRD collected on Philips X'Pert PRO diffractometer equipped with Cu-Kα radiation ($\lambda = 0.15418$ nm). The transmittance of thin films was measured using a PerkinElmer UV–VIS–NIR Lambda 19 spectrophotometer in the 190–1800 nm spectral range. The infrared absorption modes of the films were obtained from Fourier transformed infrared (FTIR) absorbance measurements recorded at room temperature using constant powder samples imbedded in KBr pellet of 5 mm diameter. The sample for FTIR measurement was prepared by grinding the thin film scraped from the glass substrate in a synthetic sapphire mortar, pestle and tableting the ground solid with KBr. The FTIR spectra were recorded using Thermo-Nicolet equipment in the 4000–400 cm$^{-1}$ region. For oxides, all bands have characteristic frequencies between 1000 and 400 cm$^{-1}$. PL measurements were taken at room temperature using a PerkinElmer LS45 luminescence spectrometer equipped with a xenon arc lamp as the excitation source. Emission spectra were recorded employing an excitation wavelength of 313 nm.

### 2.3 Optical model

The refractive index dispersion plays an important role in optical communication and designing of optical devices. Therefore, it is important to determine dispersion parameters of the films. In the transparent region (extinction coefficient $k = 0$), the dispersion parameters of the films were evaluated using a single-effective-oscillator fit, proposed by Wemple and DiDomenico [17]:

$$n^2 - 1 = \frac{\left(n_\infty^2 - 1\right)\lambda^2}{\lambda^2 - \lambda_0^2} \quad (1)$$

where $n_\infty$ and $\lambda_0$ are the high-frequency refractive index and average oscillator wave length, respectively.

When absorption bands in the visible and near infrared regions exist (extinction coefficient, $k \neq 0$), the refractive index dispersion data can be analyzed by the following dispersion relation:

$$n^2 - 1 - k^2 = \frac{\left(n_\infty^2 - 1\right)\lambda^2}{\lambda^2 - \lambda_0^2} \tag{2}$$

In the case where the experimental spectrum of a chemical system, the absorbance reveals a band of absorption "simple form," an electronic transition or charge-transfer transition are able to correctly describe the same band. A simple Gaussian profile centered on the vertical transition in question is then used to reproduce the structure of this absorption band. This assumes a vertical electronic transition between a state $S_i$ and a state $S_j$, electron transition wavelength $\lambda_{i\to j}$ and oscillator strength $f_{i\to j}$. The expression of the resulting spectral band $\alpha_{i\to j}$ is proportional to a Gaussian function such as:

$$\alpha_{i\to j}(\lambda) \propto \frac{f_{i\to j}}{\xi'\sqrt{\pi}}\exp\left(-\frac{\left(\lambda-\lambda_{i\to j}\right)^2}{\xi'^2}\right), \quad \xi' = \frac{\xi}{2\sqrt{\ln(2)}} \tag{3}$$

where $\xi$ represents the width at half maximum of the Gaussian function, or bandwidth. This parameter is chosen empirically by comparison with experiment.

The extinction coefficient $k$ is related to the absorption coefficient $\alpha$ by the expression $4\pi k/\lambda$.

The extinction coefficient $k$ in the transparent region ($\lambda \geq \lambda_g$) [18] is defined by:

$$k = k_0\frac{\left(\exp(B\,\lambda_g/\lambda) - 1\right)}{(\exp(B) - 1)} + \frac{\lambda}{4\pi}\sum_{j=1}^{q}\alpha_{i\to j}(\lambda) \tag{4}$$

where $\lambda_g$ is the wavelength of absorption region [$E_g(\text{eV}) = 1239.8/\lambda_g(\text{nm})$], $i$—ground state, $j$—excited state, and $q$ is the number of excited states.

The extinction coefficient $k$ in the region of interband transitions ($\lambda \leq \lambda_g$) is defined by:

$$k = k_1\left(1 - \frac{\lambda}{\lambda_g}\right)^r + k_0, \tag{5}$$

where $k_0$, $k_1$, $B$, $\lambda_g$, $f_{i\to j}$, $\xi'$, and $\lambda_{i\to j}$ are the fitting parameters and $r$ can have values as 1/2, 3/2, 2, and 3 depending on the nature of the interband electronic transitions, such as direct allowed, direct forbidden, indirect allowed, and indirect forbidden transitions, respectively [19, 20]. For ZnO, the value of $r$ is always 1/2, i.e., the fundamental absorption corresponds to allowed direct transition.

In order to calculate the optical constants from the obtained data, one requires formulae which relate the measured values of $T(\lambda)$ and thickness $d$, to the real and imaginary components of the refractive index, $N = n - ik$, for an absorbing film on a transparent substrate. The common approach is to consider the reflection and transmission of light at the three interfaces of the air/film/substrate/air multilayer structure and express the results in terms of Fresnel coefficients.

The system is surrounded by air with refractive index $n_0 = 1$. Taking all the multiple reflections at the three interfaces into account, it can be shown that in the case $k^2 \ll n^2$, the expression for the transmittance $T(\lambda)$ for normal incidence is given by [21–23]:

$$T = \frac{A\chi}{B - C\chi + D\chi^2} \tag{6}$$

where

$$A = 16\gamma^2 n_S(n^2 + k^2)$$

$$B = \left[(n+1)^2 + k^2\right]\left[(n+1)\left(n + n_S^2\right) + k^2\right]$$

$$C = 2\eta\left[\left(n^2 - 1 + k^2\right)\left(n^2 - n_S^2 + k^2\right) - 2k^2\left(n_S^2 + 1\right)\right]\cos\varphi - 2k\eta\left[2\left(n^2 - n_S^2 + k^2\right) + \left(n_S^2 + 1\right)\left(n^2 - 1 + k^2\right)\right]\sin\varphi$$

$$D = \eta^2\left[(n-1)^2 + k^2\right]\left[(n-1)\left(n - n_S^2\right) + k^2\right]$$

$$\varphi = 4\pi n d/\lambda$$

$$\chi = \exp(-\alpha d)$$

$$\alpha = 4\pi k/\lambda$$

$$\gamma = \exp\left[-\tfrac{1}{2}(2\pi\sigma/\lambda)^2(1-n)^2\right],\ \eta = \exp\left[-2(2\pi\sigma/\lambda)^2\right],$$

where $\sigma$ is the rms (root mean square) height of surface irregularity.

The parameters $n$ and $k$ are the real and imaginary parts of the thin film refractive index, $d$ is the film thickness, and $n_S$ is the real substrate refractive index. Knowing the refractive index of the substrate and introducing the values of $n$ and $k$ as computed from Eqs. (2), (4) and (5) into Eq. (6), the theoretical transmittance value can be obtained, referred to as $T_{\text{Theo}}$. Then, by applying Levenberg–Marquardt least-square method, the experimental transmittance data ($T_{\text{expt}}$) were fitted completely with the transmittance data calculated ($T_{\text{theo}}$) by Eq. (6) via a combination of Wemple–DiDomenico model, absorption coefficient of an electronic transition (or charge-transfer transition) and Tauc–Urbach model.

Minimizing a sum of squares ($|T_{\text{expt}} - T_{\text{theo}}|$) generated for different values of the thickness ($d$) and wavelength of gap ($\lambda_g$) by iterative technique, and finding the corresponding $n$ and $k$, the exact film thickness and energy gap can be calculated.

The refractive index of glass substrate is taken from Ref. [24]:

$$n_S^2 = 1 + \frac{1.0396 \times \lambda^2}{\lambda^2 - 6.0069 \times 10^3} + \frac{0.23179 \times \lambda^2}{\lambda^2 - 2.0017 \times 10^4} + \frac{1.0104 \times \lambda^2}{\lambda^2 - 1.0356 \times 10^8} \quad (7)$$

## 3 Results and discussion

### 3.1 Structure analysis

Figure 1 shows the evolution of XRD pattern of $Zn_{1-x}Mg_xO$ films deposited at 450 °C. The diffraction peaks are easily indexed on the basis of the hexagonal structure of ZnO (P63m/c, $a = 0.3249$ nm and $c = 0.5205$ nm, JCPDS card No. 36-1451) and the cubic structure of MgO (Fm3m, $a = 0.4211$ nm, JCPDS card No. 45-0946).

The XRD patterns reveal that the films with Mg content, $x \leq 0.10$, show highly intense (002) diffraction peak along with (101) peak which corresponds to wurtzite ZnO phase without any impurity phase (MgO, Mg or Zn). This result clearly indicated that $Mg^{2+}$ can be fully incorporated within ZnO lattice by USP with no phase segregation taking place in these films.

It can be noticed that the position of (002) reflection shifted to higher $2\theta$ angles (34.47°–34.54°) with the increase in Mg content. The lattice constant "$c$" was found to decrease with increasing Mg content from 0.520 nm ($x = 0.00$) to 0.518 nm ($x = 0.10$) indicating $c$-axis compression, while the lattice constant "$a$" monotonically increases from 0.3244 nm ($x = 0.00$) to 0.3253 nm ($x = 0.10$).

On the other side, in addition to ZnO wurtzite peaks, XRD patterns of films ($x \geq 0.21$) reveal the appearance of new peaks corresponding to MgO cubic phase, and their intensity increases with increasing Mg content. Therefore, it can be stated that 21 % of Mg can be considered as the limit concentration for the formation of (Zn, Mg)O single-phase system.

Additionally, it can be also observed that the films grow preferentially along $c$-axis [the (002) reflection has the strongest intensity] up to $x = 0.10$; afterward (101) peak starts appearing, which indicates that the films become polycrystalline for higher Mg content. It can be clearly observed that the intensity of (002) peak becomes weaker, whereas that of (101) peak becomes more intense as the Mg content increases. The presence of (002)-wurtzite reflection along with (200)-cubic reflection at $x \geq 0.21$ indicates the coexistence of two phases (ZnO and MgO).

The position of (002) and (200) peaks shifted to higher diffraction angles with the increase in Mg content, once again indicating a $c$-axis compression. The crystallite size (calculated using Sherrer's equation) gradually decreased from 35 to 19 nm by increasing Mg content.

Figure 2 shows the evolution of XRD patterns of $Zn_{1-x}Mg_xO$ films with Mg content in the range 0.13–0.17. The XRD patterns indicate that single-phase $Zn_{1-x}Mg_xO$ ($0.13 < x < 0.17$) films were grown, no traces of MgO phase can be detected. In addition, (002) reflection intensity gradually decreased by increasing Mg content except for $x = 0.15$. The position of (002) peak also shifted to lower 2θ angles (34.64°–34.38°) close to the standard peak position of bulk ZnO. The lattice constant "$c$" of $Zn_{1-x}Mg_xO$ films was found to increase (0.518–0.520 nm) with increasing Mg content then decreases to reach the value of bulk ZnO. $Zn_{1-x}Mg_xO$ films show a relatively smaller change in the lattice constant. This originates presumably from the similarity of the ionic radius between

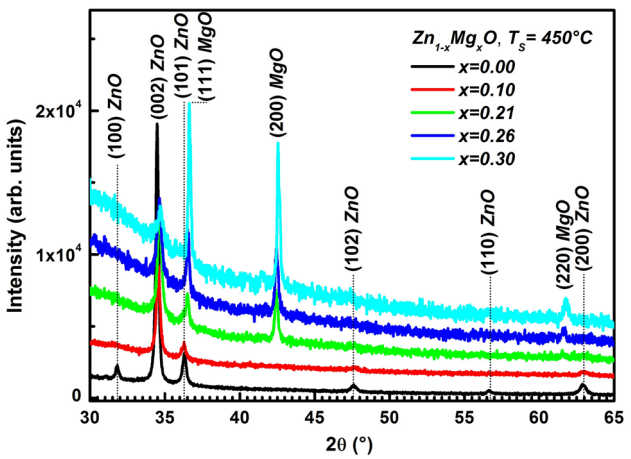


**Fig. 1** The XRD patterns of $Zn_{1-x}Mg_xO$ films with different Mg content (0, 10, 21, 26 and 30 at.%) grown onto glass substrate by ultrasonic spray pyrolysis at 450 °C

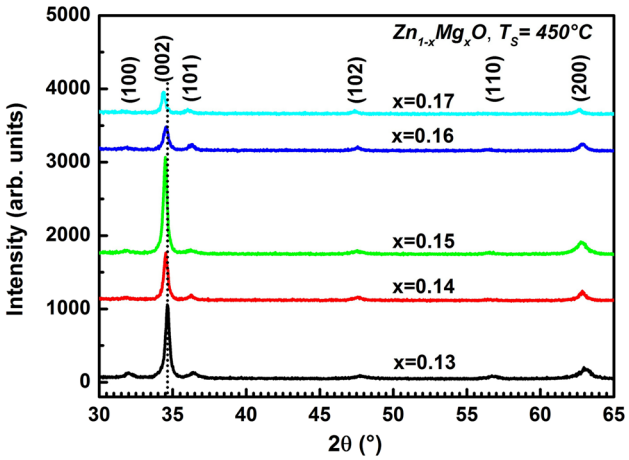


**Fig. 2** The XRD patterns of the $Zn_{1-x}Mg_xO$ films with different Mg content (13, 14, 15, 16 and 17 at.%) grown onto glass substrate by ultrasonic spray pyrolysis at 450 °C

$Zn^{2+}$(0.083 nm) and $Mg^{2+}$(0.078 nm), which can facilitate heteroepitaxial growth of ZnO/$Zn_{1-x}Mg_xO$ superlattices.

### 3.2 Microstructural observations

Figures 3 and 4 show high-resolution SEM images obtained at two magnifications; ×20,000 and ×10,000. SEM image of $Zn_{0.9}Mg_{0.1}O$ film revealed smooth surface. The distribution of columnar, hexagonal crystallites was spread almost equally all over the surface, having diameters ranging from 20 up to 100 nm. XRD (see Fig. 1) confirmed the dominance of *c*-axis-oriented wurtzite phase crystallites. At higher incorporation of Mg ($x \geq 0.21$), a drastic change in the morphology appears in agreement with the structural changes from wurtzite (ZnO) structure to a mixture of wurtzite and cubic (MgO) phases. For the film grown with $x = 0.26$, clear evidence of the formation of a cubic MgO phase can be confirmed, since pyramidal crystallites with a square/triangular base are observed. The morphology of the $Zn_{0.7}Mg_{0.3}O$ film consists of well-defined branched nanorods, having diameters in the range of 20–80 nm and lengths in the range 0.5–1 μm.

Figure 4 shows SEM images of Mg-doped ZnO thin films (13, 14, 15, 16 and 17 %) and a selected EDS spectrum of $Zn_{0.85}Mg_{0.15}O$. Doping with Mg seems to preserve the ZnO microstructure characterized by the presence of nanorods and nanopetals emerging perpendicularly to the film surface. SEM images reveal that these uniform nanograins are nanorods (or nanowire) grown mainly in the perpendicular direction of the film surface. Few nanorods can be seen also growing horizontally to the film surface. It can be noticed also the presence of nanorods in pure ZnO film (Fig. 3). Some hexagonal-like features (nanopetals/nanorods) can be observed implying the occurrence of the wurtzite ZnO crystal structure as demonstrated by XRD. In agreement with XRD results, a degradation of the crystalline properties is evidenced at higher doping level of 17 at.%, i.e., the nanostructures changes from large nanopetals to fine nanograins with reduced size below 100 nm.

The EDS spectrum of $Zn_{0.85}Mg_{0.15}O$ film reveals the different constituents O, Zn, and Mg with minor peaks

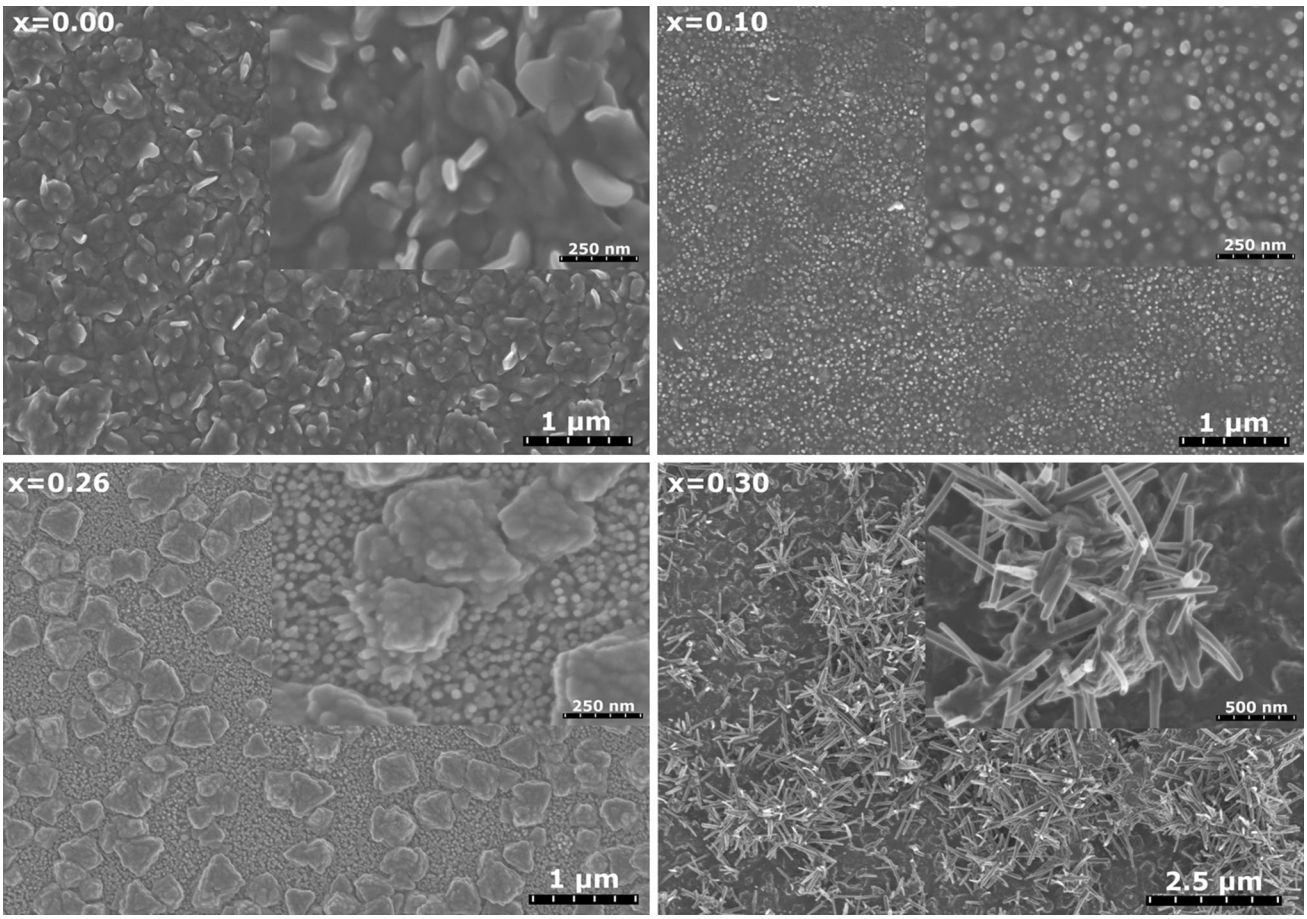


**Fig. 3** High-resolution SEM images of pure ZnO film and Mg-doped ZnO thin films. The images correspond to the Mg atomic content of 0, 10, 26 and 30 %, respectively

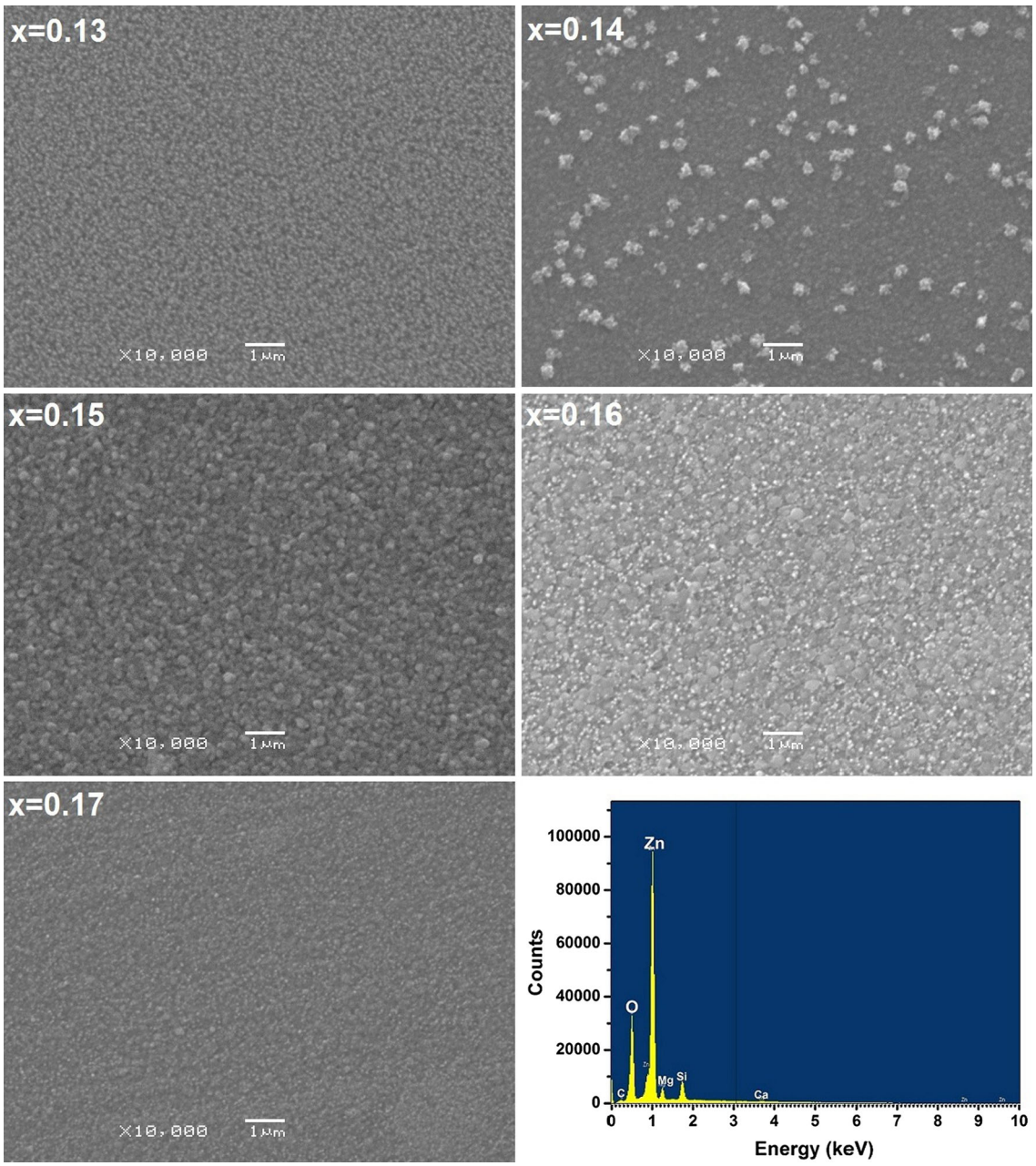


**Fig. 4** SEM images of Mg-doped ZnO thin films. The images correspond to the Mg atomic content of 13, 14, 15, 16 and 17 %, respectively, and an example of EDS spectrum recorded for $Zn_{0.85}Mg_{0.15}O$

identified as Si and Ca (belonging to soda lime glass substrate). The peak intensity of both Si and Ca varies from one sample to another, due to the variation of Mg–ZnO films' thickness. After removing the EDS background (continuum Bremsstrahlung) signal, the spectra are analyzed using Genesis Software, by considering only Zn, O and Mg peaks. The results of the chemical composition for each film are summarized in Table 1. Due to large variation of Zn content that is attributed to the variation of films' thickness and because both film and glass contains oxygen, the stoichiometry of the films is measured only from Mg and Zn signals. Let define "r" as the ratio of EDS signals of Zn and Mg and let assume stoichiometric films of the form $Zn_{1-x}Mg_xO$, the Mg atomic content $x$ can be obtained as: $x = r/(1 + r)$. Figure 5a, b show the variation of the ratio from EDS signals of Mg and Zn as well as the calculated atomic content of Mg, both plotted as function to the "expected" Mg content from the deposition. The doping with Mg is found to be effective as long as the Mg content do not exceed 16 at.%. At higher Mg

**Table 1** Composition and stoichiometry of the thin films obtained by statistical analysis of EDS spectra

| $Zn_{1-x}Mg_xO$ "Nominal" Mg content (at.) | Zn (at.%) | Mg (at.%) | O (at.%) | $x$ (Mg) "EDS" Mg content (at.) |
|---|---|---|---|---|
| $x = 0.13$ | 45.3 | 6.4 | 48.3 | 0.123 |
| $x = 0.14$ | 44.2 | 6.4 | 49.4 | 0.126 |
| $x = 0.15$ | 40.5 | 6.6 | 52.8 | 0.140 |
| $x = 0.16$ | 45.0 | 7.1 | 47.9 | 0.136 |
| $x = 0.17$ | 31.5 | 7.2 | 61.3 | 0.186 |

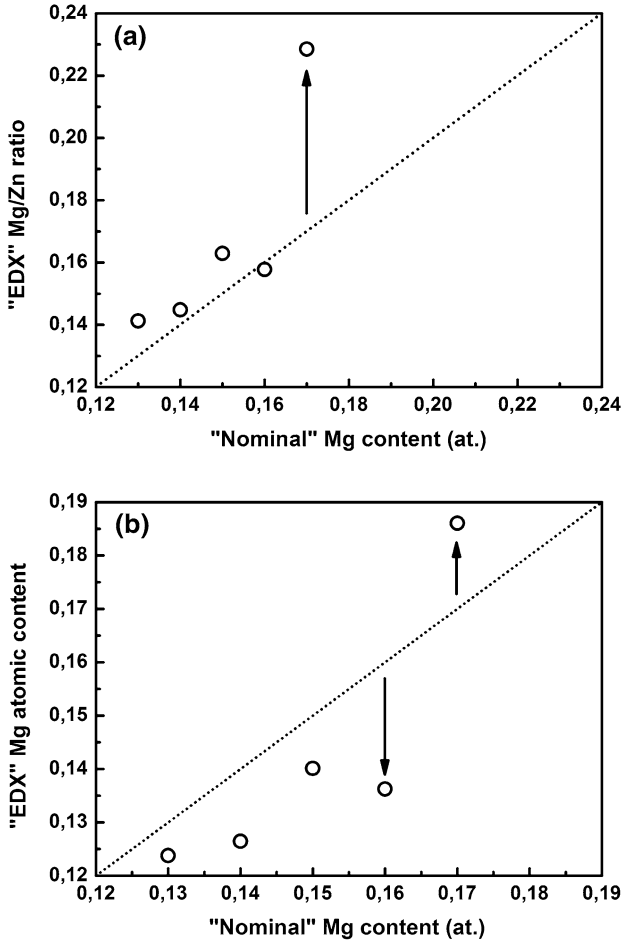


**Fig. 5** **a** The measured Mg/Zn atomic ratio and **b** the calculated Mg atomic content (from EDS analysis) plotted as function of the expected Mg content/doping

concentration, the doping is less effective and the EDS signal shows a discrepancy between the expected and measured atomic content of Mg.

### 3.3 FTIR analysis

FTIR spectroscopy will add complement the information obtained from XRD and SEM analyses. The frequencies at which absorption occurs may indicate the type of functional groups present in the substance. Figure 6 shows

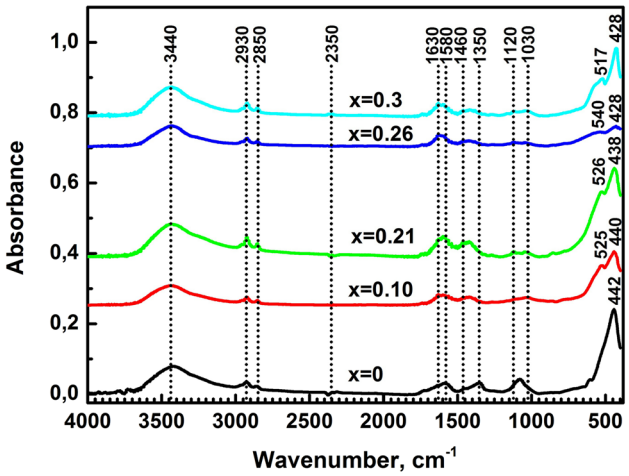


**Fig. 6** FTIR spectra of $Zn_{1-x}Mg_xO$ films grown onto glass substrate by ultrasonic spray pyrolysis at 450 °C

typical FTIR absorbance spectra of five representative $Zn_{1-x}Mg_xO$ films measured at room temperature. FTIR spectra illustrate a series of absorption bands in the range of 400–4000 $cm^{-1}$. This spectral region encompasses several important stretch modes involving hydrogen bonded to carbon as well as to oxygen, and bonding between Zn–O is clearly observed. An absorption band revealing the vibrational properties of ZnO is observed for each film in the range of 428–442 $cm^{-1}$. Common bands exist in all films, such as the broad OH band centered around 3440 $cm^{-1}$, and the 1630 $cm^{-1}$ $H_2O$ vibration band. The very high surface area of these films results in rapid adsorption of water from the atmosphere (FTIR samples were kept and ground in air). The peaks at 1350 and 1580 $cm^{-1}$ originate from the symmetric ($\nu_s$) and asymmetric ($\nu_{as}$) vibrations of the carboxyl function group ($COO^-$). For metal carboxylate complexes, the magnitude of the splitting ($\Delta$) between the $\nu_s(COO^-)$ and $\nu_{as}(COO^-)$ can be regarded as a measure for the coordination structure [25, 26]. In fact, the monodentate ligand has $\Delta > 200$ $cm^{-1}$, a bidentate chelate has $\Delta < 110$ $cm^{-1}$, and bridging ligands have intermediate values of $\Delta$ ranging between 140 and 200 $cm^{-1}$ [27]. Since the observed $\Delta$ for ZnO thin film was 230 $cm^{-1}$, the ligand configuration is assigned to the monodentate configuration. This confirms

that acetate is complexed with metal zinc, likely in the surface. The small peak at $\sim$1040 cm$^{-1}$ represents C=O deformation.

Theoretical calculations predict O–H vibrations in ZnO ranging from 3216 to 3644 cm$^{-1}$, depending on the configuration and number of hydrogen atoms in the complex [28]. The hydroxyl results from the hygroscopic nature of ZnO. The two peaks of very weak intensity observed at 2850 and 2930 cm$^{-1}$ are due to C–H stretching vibrations of alkane groups. These specific peaks correlate well with the observed frequencies of the C–$H_2$ symmetric stretch (2855 $\pm$ 10 cm$^{-1}$) and C–$H_2$ asymmetric stretch (2926 $\pm$ 10 cm$^{-1}$) of saturated hydrocarbons, respectively [29, 30]. The absorption in $\sim$2350 cm$^{-1}$ is due to the presence of $CO_2$ molecular in air. The inclusion of Mg in ZnO lattice is confirmed by the emergence of the band at around 517 $\pm$ 10 cm$^{-1}$, which is identified to be the characteristic absorption band of Mg–O stretching mode [31].

### 3.4 Optical properties

Figure 7 shows optical transmittance spectra of $Zn_{1-x}Mg_xO$ ($x$ = 0, 0.10, 0.13, 0.15, 0.16 and 0.21 at.%) films. It can be seen that the absorption edge of $Zn_{1-x}Mg_xO$ films continuously shifts to a shorter wavelength as the Mg content increases. For $Zn_{0.9}Mg_{0.1}O$ film, the average transmittance in the visible wavelength region ($\lambda$ = 400–800 nm) is greater than 84 % and presented a sharp ultraviolet cutoff.

The solid curve in Fig. 7 corresponds to the curve fitting using Eq. (6), and the symbol represents the experimental data. This figure reveals a reasonable good fitting to the experimental data, implying the accurate determination of the parameters of Eq. (6). The values of $d$, $E_g$, $n_{598}$, rms and $n_\infty$ extracted by fitting the experimental data with Eq. (6) are listed in Table 2. An obvious blue shift of the absorption edges can be observed in $Zn_{1-x}Mg_xO$.

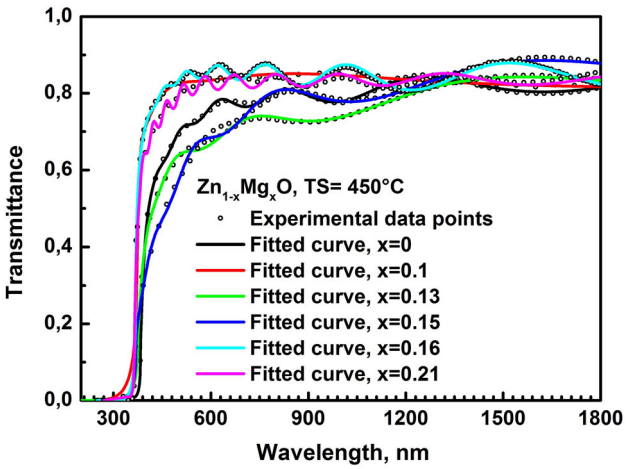


**Fig. 7** Transmission spectra of $Zn_{1-x}Mg_xO$ films deposited onto glass substrate at 450 °C. Measured (*open circles*) and calculated (*solid lines*) transmittance spectra of films

It is well known that the index of refraction is sensitive to structural defects (for example voids, dopants, inclusions), and it can provide important information concerning the microstructure of the material. The calculated refractive index of $Zn_{1-x}Mg_xO$ films versus wavelength, as shown in Fig. 8, is found to be lower than that of bulk ZnO crystal (2 at $\lambda$ = 598 nm) [17].

The plot (Fig. 9) of band gap versus Mg content shows a linear dependence with Mg content. A linear increase in the band gap [$E_g(x) = 3.227 + 0.803x$] of ZnO suggests that $Zn_{1-x}Mg_xO$ could be a suitable material for potential barrier layer in ZnO-based devices. Because $Zn_{1-x}Mg_xO$ ($x$ = 0, 10, 13, 15, 16 and 17 at.%) films have the same structure as ZnO (single wurtzite phase) with a higher $E_g$, good-quality ZnO/$Zn_{1-x}Mg_xO$ heterojunctions could be then fabricated.

### 3.5 Photoluminescence spectroscopy

It is well understood that PL spectrum usually depends on the stoichiometry and the microstructure of the film. ZnO has been known as a nonstoichiometric oxide containing O vacancy ($V_O$) and reduced interstitial Zn species. These point defects are often formed when Zn acetate transforms into ZnO during USP process. Zn acetate is a reductant whose decomposition to most stable compounds needs oxygen. ZnO is Zn-rich due to the rapid evaporation of water (source of oxygen) during growth process and the low concentration of $O_2$ in air near the substrate according to the ideal gas law. In this research work, the rapid evaporation–oxidation process, $V_O$, should be generated because of partially incomplete oxidation and crystallinity. In addition, ZnO grains with high aspect ratio (nanorods and nanopetals) should also favor the existence of high density of $V_O$ [32, 33].

Room temperature PL spectra of $Zn_{1-x}Mg_xO$ films are shown in Fig. 10. Two luminescence bands are observed: (1) One relative weak and narrow UV emission and (2) another strong and broad green (blue) emission band. Similar to the blue shift in the absorption band edge in the transmittance spectra with Mg doping, a likewise blue shift in the near-band-edge (NBE) emission is also observed.

By optimizing the peak position and half width of the Gaussian peaks, it was possible to obtain a good fit for the multi-peak combination. The Gaussian peaks (dashed lines) are shown at the bottom of Fig. 11a, b, while the solid lines represent the linear combination of the multi-Gaussian peaks with a constant background. The peak positions are marked. Mathematical treatment of PL spectra has

**Table 2** Dispersion parameters of the films extracted by fitting the experimental data with Eq. (6)

| Composition | Thickness (nm) | $E_g$ (eV) | $n$ at 598 nm | $n_\infty$ | $\sigma$ (nm) |
|---|---|---|---|---|---|
| ZnO | 705 | 3.235 | 1.779 | 1.740 | 65 |
| $Zn_{0.90}Mg_{0.10}O$ | 235 | 3.304 | 1.647 | 1.602 | 0 |
| $Zn_{0.87}Mg_{0.13}O$ | 404 | 3.308 | 1.779 | 1.762 | 33 |
| $Zn_{0.85}Mg_{0.15}O$ | 440 | 3.353 | 1.826 | 1.808 | 32 |
| $Zn_{0.84}Mg_{0.16}O$ | 829 | 3.367 | 1.885 | 1.826 | 96 |
| $Zn_{0.79}Mg_{0.21}O$ | 1204 | 3.402 | 1.684 | 1.626 | 0 |

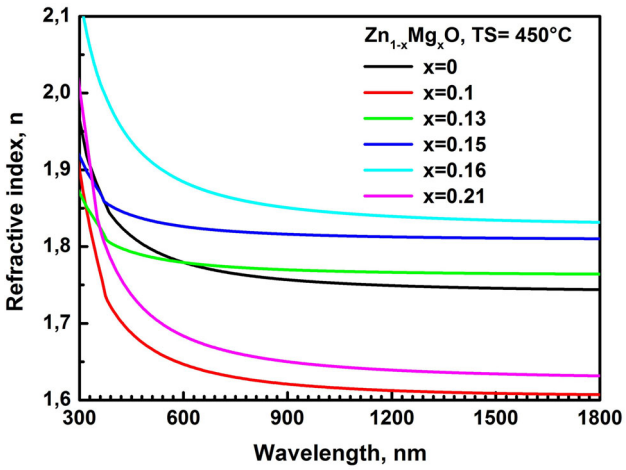


**Fig. 8** Refractive index of $Zn_{1-x}Mg_xO$ films deposited onto glass substrate at 450 °C

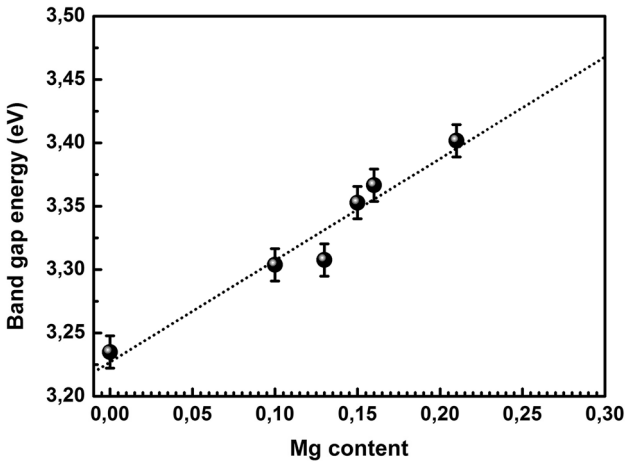


**Fig. 9** Variation of the band gap as a function of Mg content

shown that wide VIS-band consists of a series of overlapping bands. Three dominating bands are characterized by ~2.36, ~2.53, and ~2.86 eV. With the increase in Mg content, a blue shift in the peak position of the PL band was observed. The peak position of NBE varies from 3.21 eV (a) to 3.29 eV (b), and the blue shift was about 80 meV. The full widths at half maximum are 177 and 153 meV, respectively.

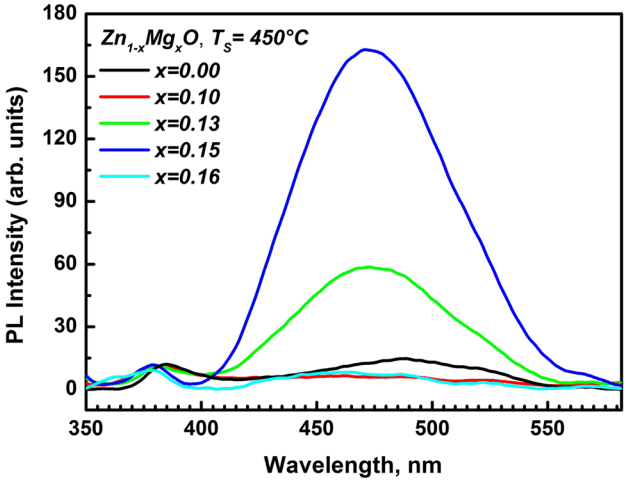


**Fig. 10** Room temperature photoluminescence spectra of $Zn_{1-x}Mg_xO$ ($x = 0$, 10, 13, 15 and 16 at.%) films

Vanheusden et al. [34] found that the intensity of the green luminescence ranging from 2.34 to 2.53 eV in ZnO correlates very well with the paramagnetic single-ionized oxygen-vacancy density, by the electron paramagnetic resonance (EPR) measurements. Only the single-ionized state can give rise to the green emission.

Based on this founding and our experimental results in Fig. 11, the singly ionized $V_O$ defects may be considered as a source for the green emissions at 2.53 eV observed in this work. The oxygen vacancies within ZnO can produce two defect donor levels, the deep level at 1.3–1.6 eV and the shallow level at 0.3–0.5 eV below the conduction band [35]. The energy difference between this latter level and the valence band is 2.8 eV, which is consistent with the photon energy of the blue emission observed in this study after the deconvolution of PL spectra. Consequently, the blue emission at around 2.86 eV may be caused by the electron transition from the shallow donor level of an oxygen vacancy to the valence band.

Figure 11b shows that there are two bands in the PL spectrum of $Zn_{0.85}Mg_{0.15}O$ thin film; one related to the UV emission at 3.29 eV and the other related to a broad visible emission (strong blue-green emission) between 2.1 and 3.1 eV and centered at 2.63 eV which is commonly

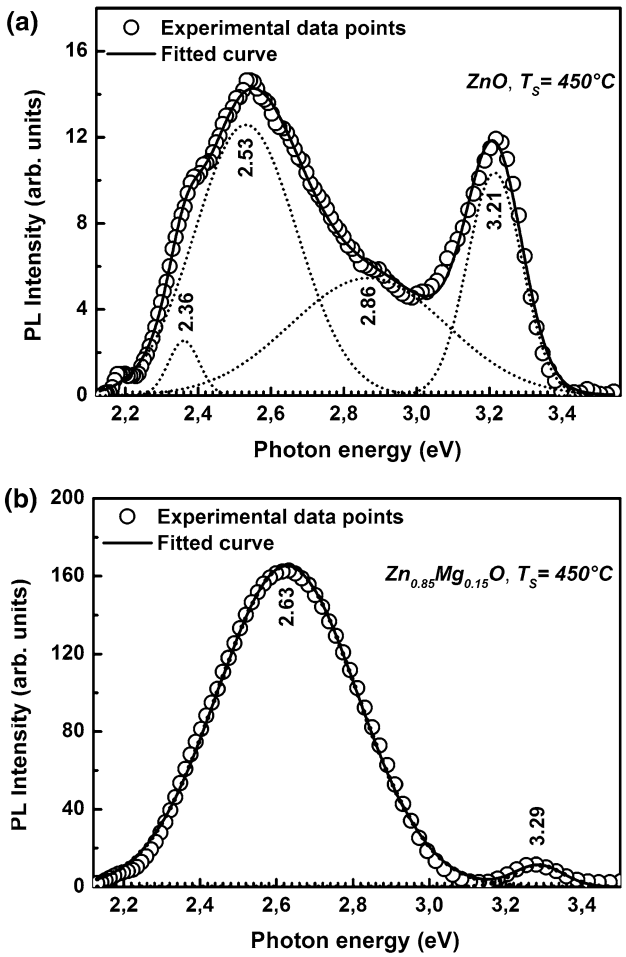


**Fig. 11** PL spectra of ZnO and $Zn_{0.85}Mg_{0.15}O$ thin films measured at room temperature. Gaussian deconvolution components (*dashed lines*) and the fit to the data (*thin solid line*) are shown

attributed to the neutral oxygen vacancies within ZnO [32]. For instance, the luminescence intensity at 2.63 eV of $Zn_{0.85}Mg_{0.15}O$ thin film is approximately 13 times higher than that of undoped ZnO film measured under the same excitation conditions. $Zn_{0.85}Mg_{0.15}O$ can serve as buffer layer, thanks to strong blue-green emission, and can replace both i-ZnO and CdS in heterojunction solar cells.

## 4 Conclusion

$Zn_{1-x}Mg_xO$ thin films have been grown onto glass substrate by USP technique using zinc acetate dihydrate and magnesium acetate tetrahydrate as Zn and Mg precursors dissolved in methanol, ethanol, and deionized water. The films were deposited at a substrate temperature of 450 °C with different Mg-doping concentration (0–0.3). The Mg doping into ZnO is found to influence considerably the film morphology, the grain size and the stoichiometry of the oxide. The nanostructure of the films is typically characterized by the presence of nanopetals and nanorods sometimes showing a hexagonal-like shape indicating wurtzite ZnO crystal structure. The doping effectiveness was revealed by EDS analysis of the chemical composition of the films, which reveals a good agreement between the expected and the measured Mg atomic content. It is found that when $x \leq 0.17$, $Zn_{1-x}Mg_xO$ thin films crystallize within a single hexagonal wurtzite ZnO structure. However, both wurtzite (ZnO) and cubic (MgO) phases were observed for $Zn_{1-x}Mg_xO$ ($x = 0.26$). FTIR study indicated the existence of distinct characteristic absorption peaks at $\sim 442$ cm$^{-1}$ for Zn–O stretching mode that shifted toward the red region with the increase in Mg content. The incorporation of Mg within ZnO lattice is confirmed by the emergence of a new band at around 523 cm$^{-1}$, which is identified to be the characteristic absorption band of Mg–O stretching mode. The optical constants and thickness of thin films have been determined using experimental transmittance data. Like the blue shift in the absorption band edge in transmittance spectra with Mg doping, a likewise blue shift in the NBE emission is also observed. The obtained results indicate that $Zn_{0.85}Mg_{0.15}O$ can be used as buffer layer, thanks to the strong blue-green emission, and hence can replace both i-ZnO and CdS in heterojunction solar cells.

**Acknowledgments** The authors would like to thank the National Project Research (PNR) and LASPI2A Laboratory of Khenchela University (Algeria) for their financial support of this research project.

## References

1. Y. Sun, J.B. Ketterson, G.K.L. Wong, Excitonic gain and stimulated ultraviolet emission in nanocrystalline zinc-oxide powder. Appl. Phys. Lett. **77**, 2322 (2000)
2. D.M. Bagnall, Y.F. Chen, Z. Zhu, T. Yao, S. Koyama, M.Y. Shen, T. Goto, Optically pumped lasing of ZnO at room temperature. Appl. Phys. Lett. **70**, 2230 (1997)
3. Z.K. Tang, G.K.L. Wong, P. Yu, M. Kawasaki, A. Ohtomo, H. Koinuma, Y. Segawa, Room-temperature ultraviolet laser emission from self-assembled ZnO microcrystallite thin films. Appl. Phys. Lett. **72**, 3270 (1998)
4. W.I. Park, G.C. Yi, H.M. Jang, Metalorganic vapor-phase epitaxial growth and photoluminescent properties of $Zn_{1-x}Mg_xO$ ($0 \leqslant x \leqslant 0.49$) thin films. Appl. Phys. Lett. **79**, 2022 (2001)
5. D.C. Look, Recent advances in ZnO materials and devices. Mater. Sci. Eng., B **80**, 383 (2001)
6. A. Ohtomo, M. Kawasaki, T. Koida, K. Masabuchi, H. Koinuma, Y. Sakurai, Y. Yoshida, T. Yasuda, Y. Segawa, $Mg_xZn_{1-x}O$ as a II–VI widegap semiconductor alloy. Appl. Phys. Lett. **72**, 2466 (1998)
7. Th Gruber, C. Kirchner, R. Kling, F. Reuss, A. Waag, F. Bertram, D. Forster, J. Christen, M. Schreck, Optical and structural analysis of ZnCdO layers grown by metalorganic vapor-phase epitaxy. Appl. Phys. Lett. **83**, 3290 (2003)

8. Y.R. Ryu, T.S. Lee, J.A. Lubguban, A.B. Corman, H.W. White, J.H. Leem, M.S. Han, Y.S. Park, C.J. Youn, W.J. Kim, Wide-band gap oxide alloy: BeZnO. Appl. Phys. Lett. **88**, 052103 (2006)
9. T. Minemoto, Y. Hashimoto, T. Satoh, T. Negami, H. Takakura, Y. Hamakawa, Cu(In, Ga)$Se_2$ solar cells with controlled conduction band offset of window/Cu(In, Ga)$Se_2$ layers. J. Appl. Phys. **89**, 8327 (2001)
10. C. Platzer-Björkman, T. Törndahl, A. Hultqvist, J. Kessler, M. Edoff, Optimization of ALD-(Zn, Mg)O buffer layers and (Zn, Mg)O/Cu(In, Ga)$Se_2$ interfaces for thin film solar cells. Thin Solid Films **515**, 6024 (2007)
11. T. Makino, Y. Segawa, M. Kawasaki, A. Ohtomo, R. Shiroki, K. Tamura, T. Yasuda, H. Koinuma, Band gap engineering based on $Mg_xZn_{1-x}O$ and $Cd_yZn_{1-y}O$ ternary alloy films. Appl. Phys. Lett. **78**, 1237 (2001)
12. X. Zhang, X.M. Li, T.L. Chen, J.M. Bian, C.Y. Zhang, Structural and optical properties of $Zn_{1-x}Mg_xO$ thin films deposited by ultrasonic spray pyrolysis. Thin Solid Films **492**, 248 (2005)
13. P. Bhattacharya, R.R. Das, R.S. Katiyar, Comparative study of Mg doped ZnO and multilayer ZnO/MgO thin films. Thin Solid Films **447**, 564 (2004)
14. A. Singh, A. Vij, D. Kumar, P.K. Khanna, M. Kumar, S. Gautam, K.H. Chae, Investigation of phase segregation in sol–gel derived ZnMgO thin films. Semicond. Sci. Tech. **28**, 025004 (2013)
15. K. Koike, K. Hama, I. Nakashima, G.Y. Takada, K.I. Ogata, S. Sasa, M. Inoue, M. Yano, Molecular beam epitaxial growth of wide bandgap ZnMgO alloy films on (111)-oriented Si substrate toward UV-detector applications. J. Cryst. Growth **278**, 288 (2005)
16. S. Choopun, R.D. Vispute, W. Yang, R.P. Sharma, T. Venkatesan, H. Shen, Realization of band gap above 5.0 eV in metastable cubic-phase $Mg_xZn_{1-x}O$ alloy films. Appl. Phys. Lett. **80**, 1529 (2002)
17. S.H. Wemple, M. DiDomenico Jr, Behavior of the electronic dielectric constant in covalent and ionic materials. Phys. Rev. B **3**, 1338 (1971)
18. S. Roguai, A. Djelloul, C. Nouveau, T. Souier, A.A. Dakhel, M. Bououdina, Structure, microstructure and determination of optical constants from transmittance data of co-doped Zn 0.90 Co 0.05 M 0.05 O (M Al, Cu, Cd, Na) films. J. Alloys Compd. **599**, 150 (2014)
19. J. Tauc, in *Optical Properties of Solids*, ed. by F. Abeles (North-Holland, Amsterdam, 1970) p. 277
20. E.A. Davis, N.F. Mott, Conduction in non-crystalline systems V. Conductivity, optical absorption and photoconductivity in amorphous semiconductors. Philos. Mag. **22**, 903 (1970)
21. R. Swanepoel, Determination of surface roughness and optical constants of inhomogeneous amorphous silicon films. J. Phys. E: Sci. Instrum. **17**, 896 (1984)
22. A.K. Aqili, A. Maqsood, Determination of thickness, refractive index, and thickness irregularity for semiconductor thin films from transmission spectra. Appl. Opt. **41**, 218 (2002)
23. J. Szczyrbowski, A. Czapla, Optical absorption in DC sputtered InAs films. Thin Solid Films **46**, 127 (1977)
24. http://refractiveindex.info/?group=GLASSES&material=BK7
25. P.C. Hidber, T.J. Graule, L.J. Gauckler, Citric acid—a dispersant for aqueous alumina suspensions. J. Am. Ceram. Soc. **79**, 1857 (1996)
26. G. Socrates, *Infrared and Raman characteristic group frequencies*, 3rd edn. (Wiley, New York, 2001), p. 347
27. K. Nakamoto, *Infrared and Raman spectra of inorganic and coordination compounds* (Wiley, New York, 1986), p. 231
28. E.V. Lavrov, J. Weber, F. Börrnert, C.G. Van de Walle, R. Helbig, Hydrogen-related defects in ZnO studied by infrared absorption spectroscopy. Phys. Rev. B **66**, 165205 (2002)
29. N.H. Nickel, K. Fleischer, Hydrogen local vibrational modes in zinc oxide. Phys. Rev. Lett. **90**, 197402 (2003)
30. G.-C. Yi, B.W. Wessels, Carbon–hydrogen complexes in vapor phase epitaxial GaN. Appl. Phys. Lett. **70**, 357 (1997)
31. C.J. Pan, H.C. Hsu, H.M. Cheng, C.Y. Wu, W.F. Hsieh, Structural and optical properties of ZnMgO nanostructures formed by Mg in-diffused ZnO nanowires. J. Solid State Chem. **180**, 1188 (2007)
32. K. Bouzid, A. Djelloul, N. Bouzid, J. Bougdira, Electrical resistivity and photoluminescence of zinc oxide films prepared by ultrasonic spray pyrolysis. Phys. Status Solidi A **206**, 106 (2009)
33. A. Djelloul, M.S. Aida, J. Bougdira, Photoluminescence, FTIR and X-ray diffraction studies on undoped and Al-doped ZnO thin films grown on polycrystalline α-alumina substrates by ultrasonic spray pyrolysis. J. Lumin. **130**(11), 2113 (2010)
34. K. Vanheusden, W.L. Warren, C.H. Seager, D.R. Tallant, J.A. Voigt, B.E. Gnade, Mechanisms behind green photoluminescence in ZnO phosphor powders. J. Appl. Phys. **79**, 7983 (1996)
35. D.H. Zhang, Z.Y. Xue, Q.P. Wang, The mechanisms of blue emission from ZnO films deposited on glass substrate by rf magnetron sputtering. J. Phys. D **35**, 2837 (2002)